American Mineralogist, Volume 66, pages 127–141, 1981

Exsolution relationships in a clinopyroxene of average composition $Ca_{0.43}Mn_{0.69}Mg_{0.82}Si_2O_6$: X-ray diffraction and analytical electron microscopy[1]

WENDY A. GORDON,[2] DONALD R. PEACOR, PHILIP E. BROWN, ERIC J. ESSENE

Department of Geological Sciences
University of Michigan, Ann Arbor, Michigan 48109

AND LAWRENCE F. ALLARD

Department of Materials and Metallurgical Engineering
University of Michigan, Ann Arbor, Michigan 48109

Abstract

A pyroxene of average composition $Ca_{0.43}Mn_{0.69}Mg_{0.82}Si_2O_6$ from Balmat, New York is exsolved to coexisting $P2_1/c$ and $C2/c$ phases. Structure refinements were performed in part to limit the compositions of the individual phases, as were plots of cell parameters and average M1–O and M2–O bond distances *vs.* composition. Site occupancies showed that the phases are manganoan diopside and kanoite. Transmission electron micrographs revealed that the phases are lamellar, share (001) as the interphase boundary, and are 2000Å wide. X-ray energy dispersive analysis of individual lamellae yielded $Ca_{0.68}Mn_{0.44}Mg_{0.88}Si_2O_6$ for the $C2/c$ phase and $Ca_{0.12}Mn_{1.02}Mg_{0.86}Si_2O_6$ for the $P2_1/c$ phase. Dark-field imaging revealed the presence of antiphase domain boundaries in the $P2_1/c$ phase, indicating the existence of a $C2/c$–$P2_1/c$ transition for the Ca-poor phase in the Ca–Mn–Mg pyroxene system. *In situ* heating experiments yield a temperature of the $C2/c$–$P2_1/c$ inversion of 330±20°C. Observation of antiphase boundary (APB) positions before and after heating through the inversion temperature showed that the APB positions were essentially unchanged, indicating stabilization of APB's by the concentration of Ca or some defect at the APB's. Lattice fringe images across the lamellar boundary (001) indicate that the interface is semi- or completely coherent. The features of this exsolution texture are consistent with initial exsolution by spinodal decomposition or nucleation and subsequent slow cooling in a regionally metamorphosed phase.

Introduction

In the investigation of a magnesian rhodonite from Balmat Mine No. 4, New York (Peacor *et al.*, 1978), a pyroxene coexisting with the rhodonite was qualitatively analyzed and determined to have major Mn and Mg with minor Ca. This is near the ideal composition of kanoite, $MnMgSi_2O_6$ (Kobayashi, 1977). Quantitative wavelength dispersive analyses on the electron microprobe were obtained for this pyroxene (Table 1). A pale blue schiller observed in the Mn-pyroxene indicated the presence of a periodic microstructure, and preliminary single-crystal and powder X-ray diffraction photographs confirmed that it did indeed consist of two pyroxenes. We report results obtained primarily through single-crystal X-ray diffraction and further characterization of the two phases by scanning transmission electron microscopy in conjunction with X-ray energy-dispersive analysis.

Our two samples, provided by the generosity of Dr. David Dill of the mine staff, consist primarily of alternating bands of bright pink rhodonite, buff-colored pyroxene, and quartz. They were found by miners at Balmat and were saved only because of their unique and colorful appearance, and are from a complexly interlayered sequence of metamorphosed, impure, siliceous carbonates and evaporites typical of the southwest part of the Grenville Province (Engel, 1956). The majority of the units consist of calcitic and dolomitic marbles with variable amounts of

[1]Contribution No. 361 from the Mineralogical Laboratory, Department of Geological Sciences, The University of Michigan.

[2]Present address: EXXON Co., U.S.A., P.O. Box 1600, Midland, Texas 79702.

0003–004X/81/0102–0127$02.00

Table 1. Electron microprobe analysis of Balmat clinopyroxene

Oxide	wt.%	Molar ratio/2Si
SiO_2	52.09	2.00
Al_2O_3	0.25	0.01
MnO	21.06	0.69
MgO	14.21	0.82
FeO	0.28	0.01
CaO	10.41	0.43
sum	98.30	

[1] Standards used were synthetic tephroite for Mn, Irving clinopyroxene for Ca and Si, Ingamell's almandine for Al and Fe, and Marjalahti olivine for Mg. Drift, atomic number, fluorescence, absorption, and background corrections were applied to the data, using the program EMPADR VII (Rucklidge and Gasparrini, 1969).

diopside, tremolite, phlogopite, calcite, anhydrite, and primary talc. Scattered Mn-rich pods have yielded the amphibole tirodite (Brown *et al.*, 1979) as well as the assemblages Mn-pyroxene–Mg-rhodonite–talc–quartz and Mn-pyroxene–Mg-rhodonite–manganoan calcite–quartz–anhydrite. The Balmat ore deposit has been regionally metamorphosed, the peak metamorphic event there being estimated at $P = 6.5 \pm .5$ kbar and $T = 625 \pm 25$°C, as calculated from sphalerite barometry (Brown *et al.*, 1978), two-feldspar, iron–titanium oxide, and calcite–dolomite thermometry (Bohlen and Essene, 1977; Brown *et al.*, 1978), and from the presence of sillimanite in the adjacent metapelites.

Determination of lattice parameters

Cleavage fragments of the pyroxene were examined by Weissenberg and precession techniques. Two reciprocal lattices were observed in the diffraction photographs; characterization of the extinction rules combined with identification of the phases as pyroxenes led to the assignment of space groups $P2_1/c$ and $C2/c$. The class (b) ($h+k=2n+1$) reflections of the primitive phase were sharp, with no diffuseness or streaking.

A powder diffractometer pattern obtained with quartz as an internal standard, Cu$K\alpha$ radiation, and graphite monochromator, showed only single unresolved peaks, and a combination of single-crystal and powder-diffraction techniques was required to determine accurate lattice parameters. Least-squares refinement of the average lattice parameters for the two phases was carried out with the program LCLSQ, written by Charles W. Burnham. Estimates of the lattice parameters for the individual phases were then obtained by Weissenberg, precession, and Weissenberg-diffractometer techniques. Thus, precise absolute values could not be obtained, but differences in the values of corresponding parameters were applied to the average values as determined with the powder diffractometer, resulting in the final values $a = 9.78(2)$, $b = 8.93(9)$, $c = 5.32(2)$Å, $\beta = 108.60(7)°$ for the primitive phase, and $a = 9.76(2)$, $b = 8.93(9)$, $c = 5.27(2)$Å, $\beta = 106.44(4)°$ for the C-centered phase. The magnitudes of the b axes of the two phases are virtually identical, their a-axis magnitudes are only slightly different, but a significant difference exists in their values of c. The **c** axes diverge by an angle of 2.16(2)°, and **a** and **b** of the two lattices are parallel. We therefore predicted an intergrowth of these phases with (001) as the common plane of least strain, a relation verified by direct indexing of the lamellar interface.

Crystal structure refinements

Refinements of the crystal structures of the coexisting pyroxenes were carried out in part to determine the nature of the individual site occupancies, which in turn restricts the compositions of the individual phases. These refinements also provide data on the general nature of pyroxene structures as a function of composition, and specifically for two compositions which appear to have formed under equilibrium conditions.

The measurement of intensity data was difficult because the class (a) diffraction maxima from the separate lattices are poorly resolved. Intensities for these diffraction maxima could not be measured utilizing an automated system, and were determined by graphically recording intensity profiles and integrating the areas using a planimeter. Even this method failed to provide resolution for diffraction maxima with a relatively large value of the index h, and the data sets were significantly smaller than is usually the case for pyroxenes. Class (b) diffractions for the primitive phase were measured with the Supper-Pace automated system, which employs background counts on each side of a continuous peak scan. The class (b) and (a) diffraction maxima were placed on the same scale by comparing class (b) diffraction intensities as determined with both methods.

A crystal approximately $0.16 \times 0.08 \times 0.39$ mm was selected and mounted for rotation about the b axis of the Weissenberg-geometry diffractometer. Mo$K\alpha$ radiation monochromated with a flat graphite crystal was used. For the C-centered phase, 374 intensities were measured, while for the primitive

phase we determined the intensities of 982 diffractions, of which 386 were class (a). These include 139 unobserved intensities for the class (a) diffractions of the primitive phase, 27 for class (b) of the primitive phase, and 21 for the C-centered phase. Intensities were determined for reflections having $\sin\theta$ less than 0.5. All data were corrected for Lorentz, polarization, and absorption effects (μ = 38 cm^{-1}), by a modified version of the program ABSRP written by C. W. Burnham.

The structure was refined using the program RFINE2 (Finger and Prince, 1975). Form factors were those of Doyle and Turner (1968). The weighting scheme of Cruickshank (1965, p. 114) was used, and all reflections with individual discrepancy factors greater than 0.5 were rejected. For the primitive phase, separate scale factors were used for the class (a) and (b) diffractions.

Form factors were initially chosen for M1 and M2 of both phases, based only on general pyroxene crystal-chemical principles in relation to the average composition as determined by electron microprobe analysis. For the C-centered phase M1 was assumed to be occupied by Mg and Mn, and M2 by Ca and Mn. For the primitive phase Mn and Mg were both assigned to M1 and M2. These are only approximations to true site occupancies where three different cations may occupy a given site. This is especially significant for M2 of the primitive phase, which must contain some Ca in addition to Mn and Mg.

Refinement proceeded without complication through the refinement of anisotropic temperature factors. The final R values as computed including all data, both observed and unobserved, are 5.7% for the primitive phase and 5.4% for the C-centered phase. Structure factors are listed in Table 2.[3] Atom coordinates and temperature factors are listed in Table 3, thermal ellipsoid data in Table 4, selected interatomic distances in Table 5, and site occupancies in Table 6. The distances were calculated with the program ORFFE (Busing *et al.*, 1964), utilizing the full variance–covariance matrix of atomic parameters and standard errors of lattice parameters.

Discussion of refinement results

The site occupancies (Table 6) are consistent with phases near diopside and kanoite in composition. The general nature of pyroxene structure variations as a function of composition is well known; Clark *et al.* (1969) determined the details of the diopside structure, and Ghose (written communication) has

[3]To receive a copy of Table 2, order Document AM-81-147 from the Business Office, Mineralogical Society of America, 2000 Florida Avenue, NW, Washington, DC 20009. Please remit $1.00 in advance for the microfiche.

Table 3. Atom coordinates and anisotropic temperature factors for $C2/c$ manganoan diopside (above) and $P2_1/c$ kanoite (below)

Atom	x	y	z	β11	β22	β33	β12	β13	β23
M1	0	0.0929(2)	3/4	13(2)	11(3)	62(12)	0	6(3)	0
M2	0	0.7072(1)	3/4	28(1)	51(2)	86(8)	0	3(2)	0
Si	0.2114(1)	0.4075(1)	0.7635(3)	18(1)	24(2)	95(8)	-2(1)	12(2)	-4(2)
O1	0.3829(3)	0.4121(3)	0.8557(8)	18(2)	38(4)	112(20)	0(2)	11(4)	-4(5)
O2	0.1358(2)	0.2510(3)	0.6715(8)	31(3)	28(4)	164(17)	-1(2)	27(4)	-4(6)
O3	0.1489(2)	0.4812(3)	0.9994(7)	21(2)	46(4)	80(16)	-4(2)	7(4)	-16(6)
M1	0.2505(1)	0.6544(2)	0.2357(2)	13(1)	17(2)	72(7)	1(0)	2(2)	4(1)
M2	0.2534(0)	0.0235(1)	0.2332(1)	23(1)	31(1)	105(4)	3(0)	6(1)	4(1)
SiA	0.0413(1)	0.3411(2)	0.2710(3)	17(1)	19(2)	96(5)	-2(1)	11(2)	-6(2)
SiB	0.5466(1)	0.8388(2)	0.2408(3)	16(1)	21(2)	96(5)	-1(1)	11(2)	-6(2)
O1A	0.8674(3)	0.3383(4)	0.1652(9)	19(2)	23(4)	138(13)	2(2)	16(5)	9(5)
O1B	0.3726(3)	0.8382(4)	0.1367(9)	25(3)	22(4)	116(13)	1(2)	19(5)	10(5)
O2A	0.1181(3)	0.5009(4)	0.3255(9)	31(3)	26(4)	124(12)	-8(2)	16(4)	-12(5)
O2B	0.6239(3)	0.9916(4)	0.3589(9)	19(2)	38(4)	145(14)	-4(2)	9(4)	-17(5)
O3A	0.1034(2)	0.2590(3)	0.5707(6)	21(2)	41(3)	130(10)	-7(2)	12(3)	17(4)
O3B	0.6038(2)	0.7161(3)	0.4901(5)	23(2)	44(3)	112(10)	4(2)	5(3)	34(4)

Table 4. Thermal ellipsoid data for manganoan diopside and kanoite

Atom	Axis	Rms amplitude	Angle with a	Angle with b	Angle with c*
Mn-Diopside					
M1	1	0.066(7)	90	0	90
	2	0.076(4)	158(15)	90	111(15)
	3	0.091(7)	112(15)	90	21(15)
M2	1	0.098( )	60(5)	90	30(5)
	2	0.125(2)	150(5)	90	60(5)
	3	0.144(2)	90	0	90
Si	1	0.088(2)	19(9)	74(8)	80(6)
	2	0.098(3)	71(9)	156(9)	105(9)
	3	0.112(4)	95(5)	108(9)	19(8)
O1	1	0.090(5)	13(8)	91(5)	77(8)
	2	0.118(8)	81(11)	128(40)	140(37)
	3	0.128(7)	81(7)	38(40)	127(38)
O2	1	0.107(7)	92(32)	6(17)	85(9)
	2	0.113(5)	175(24)	93(33)	86(7)
	3	0.146(7)	86(6)	95(8)	7(7)
O3	1	0.089(8)	58(22)	72(6)	38(18)
	2	0.105(5)	147(22)	78(10)	60(20)
	3	0.142(6)	90(4)	22(7)	112(7)
Kanoite					
M1	1	0.072(4)	43(10)	114(14)	57(5)
	2	0.084(4)	115(11)	154(13)	96(10)
	3	0.105(3)	58(6)	100(5)	146(6)
M2	1	0.094(2)	42(3)	112(4)	56(3)
	2	0.114(2)	110(4)	158(3)	99(4)
	3	0.125(2)	55(3)	94(4)	145(3)
SiA	1	0.081(3)	50(18)	46(18)	71(4)
	2	0.089(2)	136(18)	46(18)	91(8)
	3	0.114(3)	104(4)	103(4)	19(3)
SiB	1	0.083(3)	28(12)	70(13)	71(4)
	2	0.092(3)	65(13)	153(10)	100(7)
	3	0.114(3)	103(4)	107(5)	21(4)
O1A	1	0.089(6)	36(46)	121(48)	74(7)
	2	0.096(7)	124(48)	146(45)	86(16)
	3	0.136(6)	101(6)	78(7)	16(6)
O2A	1	0.089(8)	64(8)	35(8)	69(7)
	2	0.125(5)	153(15)	63(16)	89(37)
	3	0.131(6)	99(35)	110(21)	21(8)
O3A	1	0.087(5)	26(5)	65(6)	85(6)
	2	0.114(5)	78(8)	127(7)	39(6)
	3	0.150(4)	112(3)	47(6)	51(6)
O1B	1	0.089(9)	79(20)	21(12)	108(9)
	2	0.102(6)	169(18)	81(19	97(11)
	3	0.125(7)	94(11)	71(9)	19(9)
O2B	1	0.088(6)	30(9)	74(8)	66(6)
	2	0.118(7)	65(9)	147(8)	110(9)
	3	0.148(6)	105(5)	118(8)	32(7)
O3B	1	0.084(5)	62(8)	119(5)	42(4)
	2	0.111(4)	149(7)	118(6)	77(7)
	3	0.157(5)	103(4)	42(5)	51(4)

refined a pyroxene structure near ideal kanoite in composition. We therefore shall not describe the details of the structures beyond the parameters given in the tables, except to point out the well-defined 7-fold coordination of M2 in kanoite.

The structure refinements were performed in part to limit the compositions of the individual phases. The refined compositions correspond to $Ca_{0.87}Mn_{0.19}Mg_{0.94}Si_2O_6$ for the $C2/c$ phase, and $Mn_{0.97}Mg_{1.03}Si_2O_6$ for the $P2_1/c$ phase, as calculated based only on occupancy factors, which were artifically constrained as described above. The relative volumes of the two phases were determined from preliminary transmission electron micrographs, which confirmed that the phases were indeed lamellar in nature. The computed average weighted composition, considering relative volumes, did not, however, agree satisfactorily with the observed average microprobe composition. The compositions are plotted in Figure 1. Part of this discrepancy is related to the limiting assumptions made about cation distributions for the two phases. We therefore concluded that although the site occupancies correctly indicated that the phases were near diopside and kanoite in composition, details regarding site occupancies remained to be determined.

The average M1–O and M2–O bond distances were also used to determine site occupancies. Interatomic distances as functions of composition were examined for compositional ranges of M1 and M2 of

Table 5. Selected cation–oxygen interatomic distances for kanoite and manganoan diopside

Kanoite		Mn-Diopside	
M1-O2A	2.045(4)	M1-O2	2x2.056(3)
O2B	2.066(3)	O1	2x2.068(4)
O1A	2.077(5)	O1	2x2.140(3)
O1B	2.087(4)		
		ave.	2.088
O1A	2.166(4)		
O1B	2.190(4)		
ave.	2.105		
M2-O2B	2.122(4)	M2-O2	2x2.271(4)
O2A	2.161(4)	O1	2x2.307(3)
O1B	2.177(4)	O3	2x2.613(3)
O1A	2.197(3)	O3	2x2.788(3)
O3A	2.421(3)		
O3B	2.715(3)	ave.	2.495
O3B	2.865(3)		
ave.	2.380		
SiA-O2A	1.595(4)	Si-O2	1.590(3)
O1A	1.612(4)	O1	1.605(3)
O3A	1.648(3)	O3	1.666(3)
O3A	1.682(3)	O3	1.677(3)
ave.	1.634	ave.	1.635
SiB-O2B	1.588(4)		
O1B	1.613(4)		
O3B	1.673(3)		
O3B	1.675(3)		
ave.	1.637		

Table 6. Refined M1 and M2 occupancies for maganoan diopside and kanoite

Mn-Diopside		Kanoite	
M1	Mn 0.06(1)	M1	Mn 0.10(1)
	Mg 0.94		Mg 0.90
M2	Ca 0.87(2)	M2	Mn 0.86(1)
	Mn 0.13		Mg 0.14

each phase. Linear variation of bond distances with composition was assumed.

For the $P2_1/c$ phase, the range clinoenstatite–synthetic kanoite was used for both M1–O and M2–O. Data for bond distances were obtained from Morimoto *et al.* (1960) for clinoenstatite and from Ghose (written communication) for synthetic kanoite; these are the only pyroxenes for which data exist in the Ca-poor edge of the Ca–Mn–Mg quadrilateral. For M1–O the inferred occupancy of the M1 site corresponded to $(Mg_{0.89}Mn_{0.11})$, which is in excellent agreement with the refined site occupancy. For M2–O the refined bond distance value fell just beyond the range represented by the clinoenstatite–kanoite values. However, as some Ca must be present in the $P2_1/c$ phase (as it coexists with a manganoan diopside), the slightly larger value of the M2–O distance (2.30 *vs.* 2.256Å for synthetic kanoite) is entirely reasonable when the presence of Ca in M2 is considered.

For the $C2/c$ phase, the compositional range diopside–johannsenite was chosen for M1, and diopside–$C2/c$ kanoite was chosen for M2. Bond distance data from Clark *et al.* (1969) for diopside and Freed and Peacor (1967) for johannsenite were used. An M2–O interatomic distance for a theoretical $C2/c$ kanoite was generated from the linear regression equations of Ribbe and Prunier (1977) for $C2/c$ pyroxenes and effective ionic radii of Shannon and Prewitt (1969). For M1–O the inferred site occupancy corresponded to $(Mg_{0.89}Mn_{0.11})$, which agrees well with the refined value for that site. This method was not entirely applicable to M2 of the $C2/c$ phase, as Ribbe and Prunier (1977) have shown that the M2–O distance in $C2/c$ pyroxenes is not a function of the ionic radius of M2 alone. Rather, it is a function of the ionic radii of both the M1 and M2 sites. Thus, as the composition of the M1 site does not change appreciably in the range diopside–kanoite, the value obtained for the M2 site occupancy of the $C2/c$ phase $(Ca_{0.98}Mn_{0.02})$ does not reflect any appreciable ionic substitution between Ca and Mn in M2. The overall results of this technique were in reasonable agreement with those of the structure refinements.

For cell parameters this same basic method was applied, with the compositional ranges clinoenstatite–$Mn_2Si_2O_6$ for $P2_1/c$ and diopside–kanoite for $C2/c$. This method had the same general limitations as the previous procedure. First, for the Ca-poor edge of the Ca–Mn–Mg quadrilateral, cell parameter data exist only for clinoenstatite (Stephenson *et al.*, 1966), synthetic $Mn_2Si_2O_6$ (Syono *et al.*, 1971), and synthetic kanoite. Second, the compositional range clinoenstatite–$Mn_2Si_2O_6$ does not account for small amounts of Ca, which are likely to be present in the $P2_1/c$ phase, and which will have a significant effect on the cell parameters. Thus, the value shown in Figure 1 for the composition of the $P2_1/c$ phase from this method is only a rough estimate. For the $C2/c$ phase the estimate of composition was more tightly constrained; average M1–O and M2–O bond distances were generated from the observed cell parameters and Shannon and Prewitt's (1969) effective ionic radii in the linear regression equations of Ribbe and Prunier (1977) for $C2/c$ pyroxenes. From these equations, M1 and M2 ionic radii were computed for the $C2/c$ phase, which in turn allowed a more accurate estimate of composition to be made for $C2/c$ than for $P2_1/c$. The results of this method are shown in Figure 1. The compositions determined for each phase corresponded to $Ca_{0.79}Mn_{0.21}Mg_{1.0}Si_2O_6$ for the

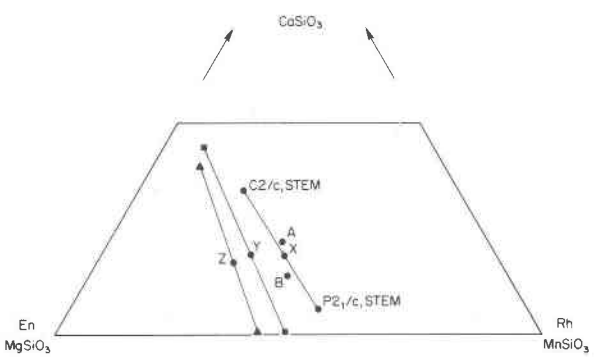

Fig. 1. Plot of Balmat $C2/c$ and $P2_1/c$ clinopyroxene compositions in the Ca–Mn–Mg quadrilateral. The points labeled A and B are average compositions for the Balmat clinopyroxene as determined from electron microprobe analyses. A corresponds to the average composition of the sample analyzed using STEM; B is included to show the range of average pyroxene compositions of the Balmat samples. ■ and ▲ represent compositions determined by structure refinements and plots of cell parameter *vs.* composition, respectively. The points labeled X, Y, and Z represent average compositions determined from the results of each method.

$C2/c$ phase, and $Mn_{0.85}Mg_{1.15}Si_2O_6$ for the $P2_1/c$ phase. The average pyroxene composition determined by this method, considering relative volumes, corresponded to $Ca_{0.34}Mn_{0.58}Mg_{1.08}Si_2O_6$, in only fair agreement with the observed average microprobe composition, although in reasonable agreement with the average refinement composition of $Ca_{0.38}Mn_{0.62}Mg_{1.00}Si_2O_6$. Nonetheless, the results of these attempts clearly underscored the necessity for some means of determining the lamellar compositions directly, which led to analysis of this material by techniques of analytical electron microscopy. Fortunately, at this stage of the study appropriate instrumentation became available to us.

Analytical electron microscopy

The electron microscope was a JEOL JEM 100CX-ASID outfitted with a Princeton Gamma-Tech energy-dispersive solid-state detector with an analytical resolution of 146 eV at 5.9 keV. This instrument combines the imaging and diffraction capabilities of the conventional (fixed beam) transmission electron microscope (CTEM) with the analytical capabilities offered by a scanning electron beam instrument (STEM). It has the capability of 2.0Å line resolution in the transmission mode, using a side-entry goniometer and the tilted beam technique for lattice fringe imagery. Incident beam diameters of 50Å and less can routinely be obtained. The actual spatial resolution for analysis, however, may be considerably increased in relatively thick samples. A thick non-beam-defining Mo aperture positioned above the specimen was used to eliminate most of the hard X-rays generated by the beam-defining aperture in the condenser system. A graphite specimen holder was used to further minimize X-rays generated in the vicinity of the sample. Nonetheless Cu$K\alpha$ was detected in all spectra, but was subsequently determined to arise from the specimen rod beneath the graphite holder. A liquid-nitrogen-cooled anti-contamination device was employed at all times to minimize organic contaminants formed at the beam–specimen interface. All electron microscopy was performed at 100 kV.

Special thin sections of the Balmat samples were made, using a glass wax that was acetone-soluble, rather than a conventional thin-section epoxy. Single crystals of pyroxene exhibiting schiller were then selected optically. The optical orientation of this pyroxene appears in general to be the same as that of the common clinopyroxene, *i.e.* the optic normal is parallel to the *b* axis. Generally the lamellae were not directly observable on the optical level, but could easily be detected with a reflected light source by the schiller. To ensure that the lamellar boundary [predicted to be (001)] would be as nearly parallel to the incident electron beam as possible, only those crystals showing centered or near-centered optic normal figures were selected. 3-mm-diameter brass washers were then attached to the crystals with a non-acetone-soluble epoxy. The crystals were subsequently removed from the slide by dissolving the glass wax with acetone, and thinned by ion bombardment using standard conditions (7 kV, 100μa Ar ion beam current, and inclination of the sample to the beams of ~15°).

From conventional transmission electron micrographs, the lamellae were seen to be approximately 2000Å wide. The interphase boundary was directly indexed as (001) within error of measurement of 1°–2°. This was accomplished through determination of the direction, [*uvw*], of the lamellae boundary for each of several different orientations. Further confirmation of this index was obtained by measuring the angle between the lamellar boundary and (110) cleavage steps seen in transmission images, which was 76°45′. Robinson *et al.* (1971) studied the orientations of exsolution lamellae in clinopyroxenes and showed that the interphase boundary of lamellae exsolved on a plane that is apparently (001) may not be parallel to (001); that is, the interface and (001) may in fact differ by an angle of as much as 10°. Therefore, the interphase boundary is actually some plane of irrational index that represents the plane of dimensional best fit between the two lattices at the time of exsolution. Our index determination, therefore, while consistent with the interphase boundary being (001), may by analogy be up to 1°–2° from the (001) plane.

Quantitative analysis

The Cliff–Lorimer (1972) simple ratio method for thin foils was used to determine the individual pyroxene compositions. This method is extremely convenient if the sample is sufficiently thin that atomic number, absorption, and fluorescence (ZAF) effects are minimal and may effectively be neglected. The ratio of characteristic X-ray intensities of two elements is therefore related to the concentration ratio of those two elements by the expression $(C_a/C_b) = k_{ab}(I_a/I_b)$. We have taken the ratio of each element present in the unknown (Mn, Mg, and Ca) to Si, assuming that only Si occupies the tetrahedral site (this was also assumed for all of the standards used). The

Nuclear Data 6600 computer system interfaced with the detector included a program which calculated the area under the curve for a chosen peak, so that the final intensity value corresponded to peak-background. Upper and lower energy levels for each peak were set manually. These computed areas were the actual values used in the intensity ratio calculations. The simple ratio method has been used successfully by other researchers on geological materials (Lorimer and Champness, 1973; Copley *et al.*, 1974; Nobugai *et al.*, 1978).

Some potential problems of chemical analysis were contamination buildup and mass loss due to volatilization, both associated with the stationary spot mode used for analysis. To check for errors from these effects, ratios of characteristic X-ray intensities were taken from the same spot every 200 seconds over a 15-minute period. This was done on the unknown and on each of nine standards. No detectable errors were found from either effect, as intensity ratios remained constant. We point out, however, that this was determined only for the materials used in this study. Care should be taken with other minerals (most notably feldspars and carbonates) to check for this effect, as mass loss may lead to serious errors in composition determinations for some phases. As an additional check for beam damage, micro–micro diffraction was performed on the individual pyroxene lamellae (*i.e.* diffraction from areas of approximately 1000 × 1000Å; Mardinly, personal communication). If specimen damage was occurring, the diffraction pattern should have gradually deteriorated due to alteration of the specimen in the beam. The resulting diffraction patterns were observed in the microscope over a period of several minutes, and were found not to change. Therefore, we concluded that sample damage from the beam was negligible.

Analysis depends on the measurement of k, a constant for each element ratio which includes corrections for the efficiency of X-ray detection by the detector (Cliff and Lorimer, 1972). To determine k values, X-ray intensity pairs for Ca/Si, Mn/Si, and Mg/Si were measured from nine homogeneous well-analyzed standards routinely used in microprobe analyses at the University of Michigan. The standards used and k values are listed in Table 7. This procedure yielded three intensity ratios for Mn/Si, four for Mg/Si, and six for Ca/Si. The k values were determined in two ways: (1) by simple calculation from the above expression, using known values of element/Si concentration in element weight percent and observed X-ray intensities; and (2) by least-squares refinement of the straight lines resulting from plots of concentration ratio *vs.* intensity ratio; the slopes of these lines are k values. There was very good agreement between k values determined from both methods. 23 analyses per standard were made, counting for 200 seconds each. The specimen holder was tilted at an angle of approximately 30° during analysis. The standards were analyzed as crushed crystals suspended on holey carbon films, because insufficient amounts of each were available with which to prepare ion-thinned standards. Care was taken to analyze only thin edges of crystal fragments in order to eliminate ZAF corrections. The plots of concentration *vs.* intensity ratios also served as checks on specimen thickness; beyond a critical thickness, ZAF effects must again be considered. As long as the relationship between concentration and intensity is linear, the simple ratio method is applicable. Note that k values must be determined for every instrument, as efficiency of X-ray detection may vary between detectors, with operating conditions, and with data reduction methods.

The lamellar compositions were determined by summing the concentrations of Ca, Mn, and Mg to one for each phase, such that the following expressions could be used:

$$C_{Ca} = [k_{CaSi}(I_{Ca}/I_{Si})]C_{Si} \quad (1)$$

$$C_{Mn} = [k_{MnSi}(I_{Mn}/I_{Si})]C_{Si} \quad (2)$$

$$C_{Mg} = [k_{MgSi}(I_{Mg}/I_{Si})]C_{Si} \quad (3)$$

Each equation is the original expression rewritten to solve for the concentration of the octahedral-site elements. Thus written, the observed intensity ratios and k values can be used to determine the Si content of each phase:

$$[k_{CaSi}(I_{Ca}/I_{Si}) + k_{MnSi}(I_{Mn}/I_{Si}) + k_{MgSi}(I_{Mg}/I_{Si})]C_{Si} = 1 \quad (4)$$

This value of C_{Si} was then used in expressions 1, 2, and 3 to solve for the contents of Ca, Mn, and Mg in each phase. Approximately 50 analyses of each of the Balmat pyroxenes were made to determine element/Si intensity ratios. Standard statistical analyses yielded the final values of k to be $k_{CaSi} = 1.27 \pm 0.09$, $k_{MnSi} = 1.399 \pm 0.002$, and $k_{MgSi} = 0.47 \pm 0.04$. The resulting errors in the STEM compositions are represented by the circles shown in Figure 1. The results of this procedure yielded compositions of $Ca_{0.68}Mn_{0.44}Mg_{0.88}Si_2O_6$ for the $C2/c$ phase, and $Ca_{0.12}Mn_{1.02}Mg_{0.86}Si_2O_6$ for the $P2_1/c$ phase. The average composition, considering relative lamellar vol-

Table 7. Standard concentration and intensity ratios used in determination of k values

Ca/Si		Mn/Si		Mg/Si	
Conc.	I	Conc.	I	Conc.	I
0.445	0.46	0.244	0.34	0.465	0.19
0.490	0.62	0.254	0.36	0.465	0.23
0.495	0.51	2.000	2.80	0.470	0.23
0.495	0.66			0.517	0.25
0.675	0.77				
0.995	1.27				

[1]Standards used were synthetic tephroite, Broken Hill bustamite, and Wabush cummingtonite for Mn/Si; Broken Hill bustamite, Ducktown diopside, Goldich diopside, ANU hedenbergite, ANU wollastonite, and Irving clinopyroxene for Ca/Si; Wabush cummingtonite, Ducktown diopside, Goldich diopside, and Irving clinopyroxene for Mg/Si. Concentration ratios for these plots were calculated in mole percent from standard analyses.

umes, corresponds to $Ca_{0.36}Mn_{0.77}Mg_{0.67}Si_2O_6$, which agrees reasonably well with the observed average microprobe composition. As predicted earlier in considering the refined compositions, the $P2_1/c$ phase does indeed contain some Ca (approximately six mole percent). The two compositions are analogous to those found in coexisting augites and pigeonites of the Ca–Mg–Fe pyroxene quadrilateral. The most obvious difference in the Ca–Mg–Mn system is the relative enrichment of the $P2_1/c$ phase in Mn. This is probably due to the marked preference of Mn for the larger M2 site, as noted by Ghose *et al.* (1975) in a study of site preferences of transition metal ions in synthetic pyroxenes. They found that, based on site occupancy refinements, Mn showed a much greater affinity for M2 than did Fe. Another major difference between the two quadrilaterals is the apparent smaller width of the solvus in the Ca–Mn–Mg system. A probable explanation for this lies with the similarity in ionic size between Ca and Mn; thus the impetus for unmixing would not be as great as that expected for Ca *vs.* Mg and Fe, where cation sizes are more disparate. The results of all methods used to determine lamellar compositions are shown in Figure 1. The compositions determined with STEM clearly give the best agreement with the observed average microprobe compositions.

Antiphase domains

The scale of antiphase domains (APD's) in pigeonites has been used by several researchers to indicate relative cooling rates (Bailey *et al.*, 1970; Christie *et al.*, 1971; Brown *et al.*, 1972; Ghose *et al.*, 1972; Lally *et al.*, 1972, 1975; Brown and Wechsler, 1973; Nord *et al.*, 1973). At high temperatures, pigeonites possess $C2/c$ symmetry, in which two chains of linked SiO_4 tetrahedra are identical. With decreasing temperature, the coordination of the cations in the M2 sites changes in concert with shifts in the chains. The chains are no longer related by symmetry, and the space group is $P2_1/c$. In pigeonites the temperature of this transformation is controlled by composition (Prewitt *et al.*, 1971). The resulting microstructure is composed of regions of the $P2_1/c$ structure (APD's) related to each other across antiphase boundaries (APB's) by a translation of $(\mathbf{a} + \mathbf{b})/2$ (Morimoto and Tokonami, 1969). The structure is thus C-centered at the boundaries.

APD size should be a function mainly of cooling rate through the inversion temperature, as the $C2/c$–$P2_1/c$ inversion in pigeonite seems to occur by random nucleation and growth of the $P2_1/c$ phase in the $C2/c$ phase. However, heterogeneous nucleation may occur and these APD's may be larger than if formed by random nucleation alone, and thus would give an erroneous indication of cooling rate (Lally *et al.*, 1975). With a relatively slow cooling rate, large APD's with fairly straight boundaries may be expected, because the few random $P2_1/c$ nuclei that form in the $C2/c$ phase have more time to grow, and straightening of boundaries is one way in which APD's can become enlarged (Cupschalk and Brown, 1968). Few instances of APD's with straight boundaries have been reported in pigeonites (Champness and Lorimer, 1971; Lally *et al.*, 1975). Carpenter (1978) describes slowly-cooled terrestrial pigeonites, which exhibit not only large APD's but also relatively straight boundaries. He cites evidence for the enrichment of some APB's in Ca, as predicted by Morimoto and Tokonami (1969). He also presents direct evidence for these APB's being good nucleation sites for augite, as noted by Lally *et al.* (1975).

As mentioned earlier, APD's on the order of 200Å or less (Morimoto and Tokonami, 1969) are revealed in single-crystal X-ray diffraction photographs by the presence of diffuseness in the class (b) reflections of the $P2_1/c$ phase. However, the class (b) reflections of our $P2_1/c$ phase were quite sharp. This was explained by bright- and dark-field transmission electron micrographs which revealed that not only were APD's present in the primitive phase, but that they were large, ranging from ~400 to ~3500Å in wdith. As no nucleation of other phases was seen in either the $P2_1/c$ or $C2/c$ phases, this coarse APD size alone in-

dicates a slow cooling rate. In any case, the large domain size allows the APD's to diffract independently, consistent with the sharp quality of the class (b) $P2_1/c$ reflections. Figure 2 shows dark-field transmission electron micrographs of the Balmat pyroxene lamellae, showing only diffraction of the $P2_1/c$ phase. The APD texture is readily apparent. The reflections used for imaging were sharp, single class (b) reflections, represented by the circled spot in the accompanying diffraction pattern (inset), which is the **a*c*** plane. Clearly, from this microtextural evidence, the Ca-poor pyroxene in the Ca–Mn–Mg quadrilateral undergoes a $C2/c$–$P2_1/c$ inversion analogous to that of pigeonites in the Ca–Mg–Fe system.

The temperature of APD inversion was qualitatively determined with a special sample heating holder in the STEM. An ion-thinned fragment of pyroxene was enclosed in a folding Cu grid, which was then placed in the heating holder. Immediately prior to heating, the APD texture was imaged in dark-field mode. Both the APD texture and the sharp class (b) imaging reflection were monitored during heating. The rate of heating and cooling was rapid (approximately 50°C per minute). As the inversion temperature was approached, the APD texture was seen to disappear quickly and continuously; concurrently, the imaging reflection was seen to decrease in intensity until it disappeared completely, as seen in the sequence shown in Figure 3. The sample was maintained above the inversion temperature (at temperatures as high as ~360°C) for no more than one to two minutes before cooling. This procedure was performed several times within a period of about 20–30 minutes. Care was taken to determine whether changes in sample inclination during thermal cycling might be causing the disappearance of both APB contrast and diffraction intensity. Bright-field observation of extinction contours, which are extremely sensitive to changes in sample tilt, indicated that the specimen remained stable during temperature changes. The results of these experiments yield a temperature of inversion corresponding to 330 ± 20°C.

Ca enrichment of APB's

In some cases, enrichment in Ca of APB's can be detected by the broadening of APB's or by the nucleation of a Ca-rich phase at the APB's (Lally *et al.*, 1975; Carpenter, 1978). We observed neither of these effects, but instead noted the distribution of the APB's which relates to the distribution of Ca, before and after heating through the inversion temperature. In Figure 4, which represents these conditions, the

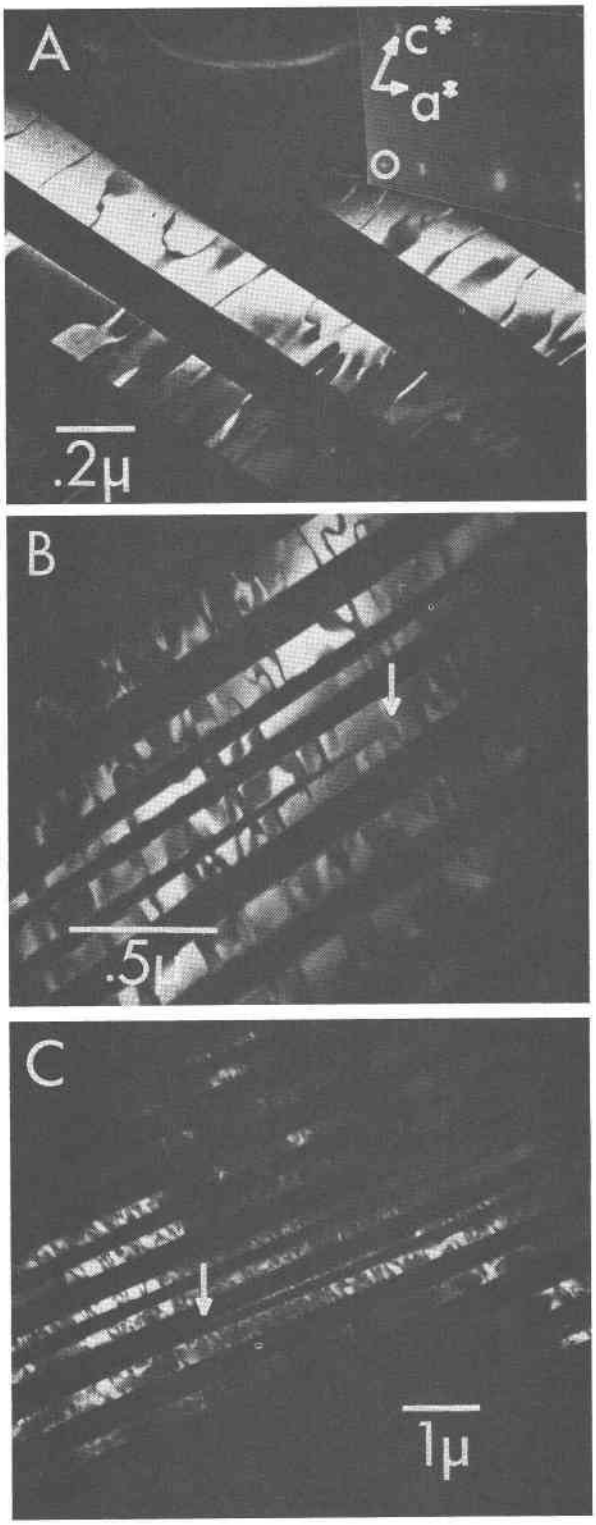

Fig. 2. Dark-field transmission electron micrographs of Balmat clinopyroxene taken at 100 kV using $h+k$ odd reflections: (A) shows diffraction pattern (inset) of **a*c*** plane, with imaging reflection circled; note the relatively large APD's and fairly straight boundaries. (B) and (C) also show "pinch-out" lamellae (arrowed) in both the $P2_1/c$ (light) and $C2/c$ (dark) lamellae.

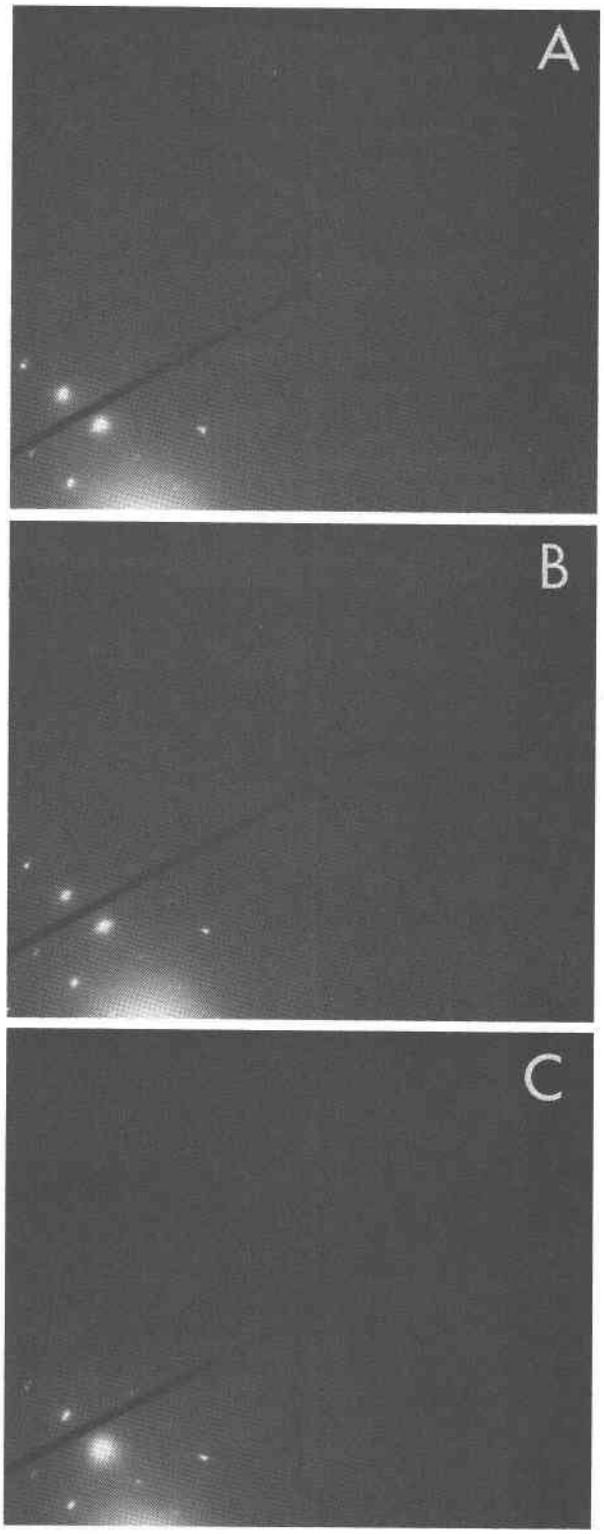

Fig. 3. Sequence showing the disappearance of $P2_1/c$ $h+k$ odd imaging reflection during heat of clinopyroxene: (A) 135°C; (B) 260°C; (C) 350°C. Diffraction patterns were taken in dark-field mode, with the electron beam tilted so that the diffracted beam is parallel to the optic axis of the microscope. All micrographs taken at 100 kV.

APB's are generally similar, even identical in several areas. This indicates that something is controlling the distribution of the APB's, giving rise to a "memory" effect after rapid heating and cooling through the inversion temperature. We concluded that Ca must be concentrated at the APB's to some extent, causing this phenomenon, although it is possible that it is caused by the presence of defects. As heating and cooling were rapid, the likelihood of appreciable diffusion of Ca away from the APB's while the sample was at a temperature above that of the inversion is small.

In an attempt to directly confirm the presence of Ca at the APB's, Ca X-ray images of lamellae showing the APD texture were recorded. A window was placed on the emission spectrum around the Ca peak in order to permit the detection of Ca$K\alpha$ photons only. These images (Fig. 5) qualitatively illustrate the enrichment of the $C2/c$ phase in Ca with respect to $P2_1/c$. Within the $P2_1/c$ phase, however, it is not possible to determine if the few Ca X-ray photons detected correlate directly to the APB's. The amount of Ca present at the APB's is simply too small to be detected relative to the inefficiency of the method. However, in light of the "memory" effect seen in the APB orientations from the heating experiments, we conclude that some Ca is probably concentrated at the APB's, and this is very likely the factor controlling the distribution of the APB's.

Coherency of the interphase boundary

From examination of the unit-cell parameters, we predicted that the index of the interphase boundary would be (001); this was subsequently verified by electron diffraction and transmission electron micrographs. This prediction was based on the fact that the greatest difference in magnitudes of parameters was between the c axes of the two pyroxenes. Both phases have the b axis in common, and a and b of the two phases are parallel. If both the a and b parameters were identical, the interphase boundary would be a coherent unstrained boundary. As the b parameters are equal within the error of observation and the a parameters are nearly equal, we thought that the lamellar interface in the sample might be such a boundary. To investigate the coherency of the interface, high-resolution electron microscopy (lattice fringe imaging) was performed using the (200) reflection.

Figure 6 shows a tilted beam lattice fringe image of (200) planes crossing the lamellar boundary. The accompanying diffraction pattern shows the **a*c*** plane, with the characteristic extinctions apparent.

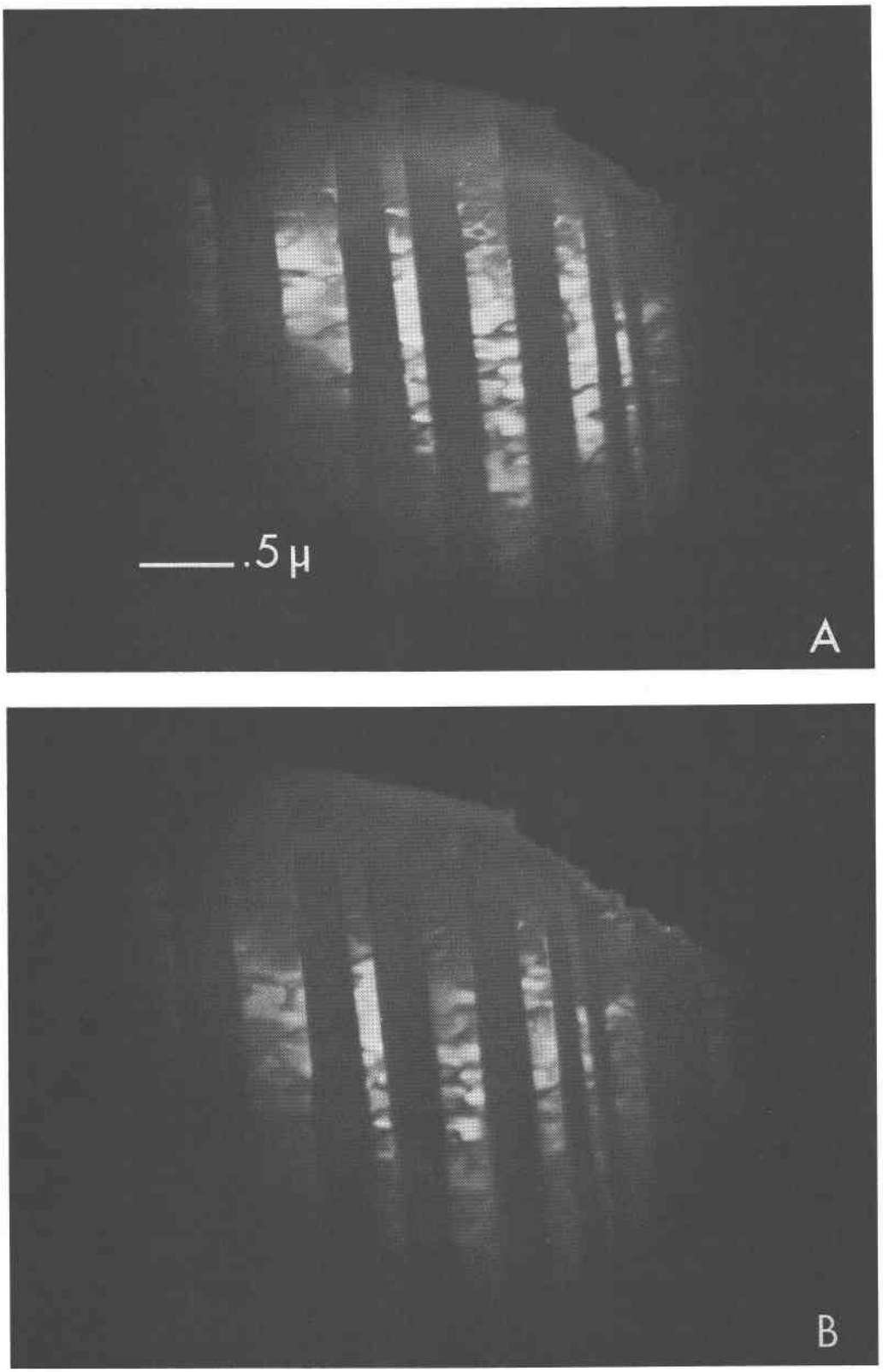

Fig. 4. Dark-field micrographs of APD's of $P2_1/c$ phase: (A) before heating; (B) after rapid heating (to 350°C) and cooling. Note the extremely similar orientations of APB's in both micrographs (100 kV).

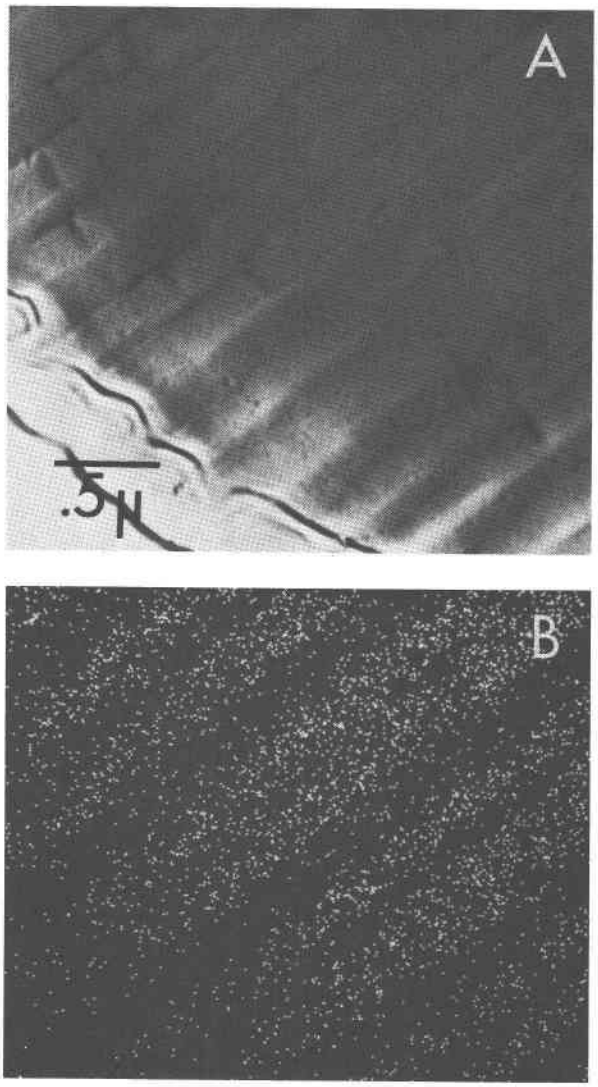

Fig. 5. (A) Scanning transmission image of clinopyroxene lamellae (lighter lamellae are $C2/c$); (B) scanning transmission Ca X-ray image of same area as in (A), showing $C2/c$ lamellae enriched in Ca; 100 kV.

The central beam and the (200) reflection used to image the 4.6Å periodic fringes are circled. In this image, it is possible to follow these fringes without interruption across the interface, at which point they bend slightly. The angle between the fringes from one phase to the other is 2.5°, which is equal to the angle between the **c** axes within error of measurement. Viewing the structure in this orientation (**b*** parallel to the incident electron beam) is essentially equivalent to observing the tetrahedral–octahedral layers of the pyroxene structure, *i.e.* the planes of closest-packed oxygen anions. From these observations, it appears that this interface must be a largely coherent boundary. The lattice parameters parallel to the interface are so similar, however, that a minimum strain condition would exist if the interface was largely coherent with dislocations separated by approximately 1000Å, a situation which would require that the interface be defined as semicoherent.

Discussion of the exsolution texture

The Balmat clinopyroxene lamellae are homogeneous phases, share (001), and are approximately 2000Å wide. The interphase boundary, as described above, is largely coherent with little strain, and the presence of APD's indicates the existence of a $C2/c$–$P2_1/c$ inversion for the Ca-poor phase. The Balmat samples exhibit an exsolution phenomenon formed completely as a product of regional metamorphism, with a well-defined and simple thermal history. The parent material for this rock was shallow marine sediment. The probable geologic sequence involved heating and crystallization of sediments by regional metamorphism to the peak temperature of 625°C and pressure of 6.5 kbar (Brown *et al.*, 1978); formation of the pyroxene, which was presumably homogeneous at the peak of metamorphism; and subsequent slow cooling from peak metamorphic conditions which permitted the pyroxene to unmix continuously to two $C2/c$ phases, one Ca-rich and one Ca-poor. Further slow cooling then allowed the Ca-poor phase to invert from $C2/c$ to $P2_1/c$ symmetry, with the associated formation of relatively large APD's. Another feature of the exsolution texture is the "pinching-out" of lamellae (Fig. 7), which occurs in both phases. A possible mechanism for formation of this feature is described by Copley *et al.* (1974); it includes phase nucleation and subsequent lamellar growth by the propagation of ledges along the interphase surface. In our sample, however, these ledges may simply be a strain-release mechanism after the formation of a dislocation, and may not necessarily be the result of heterogeneous nucleation.

We cannot assign a specific mechanism of exsolution using only the observed microstructure, although spinodal decomposition is certainly possible. Features of the microstructure are consistent with the known geologic history of the sample, especially the mostly coherent lamellar boundary, the large size of the APD's, and the apparent Ca-enrichment of APB's. Of special interest is the small amount of strain associated with the lamellar boundary, which

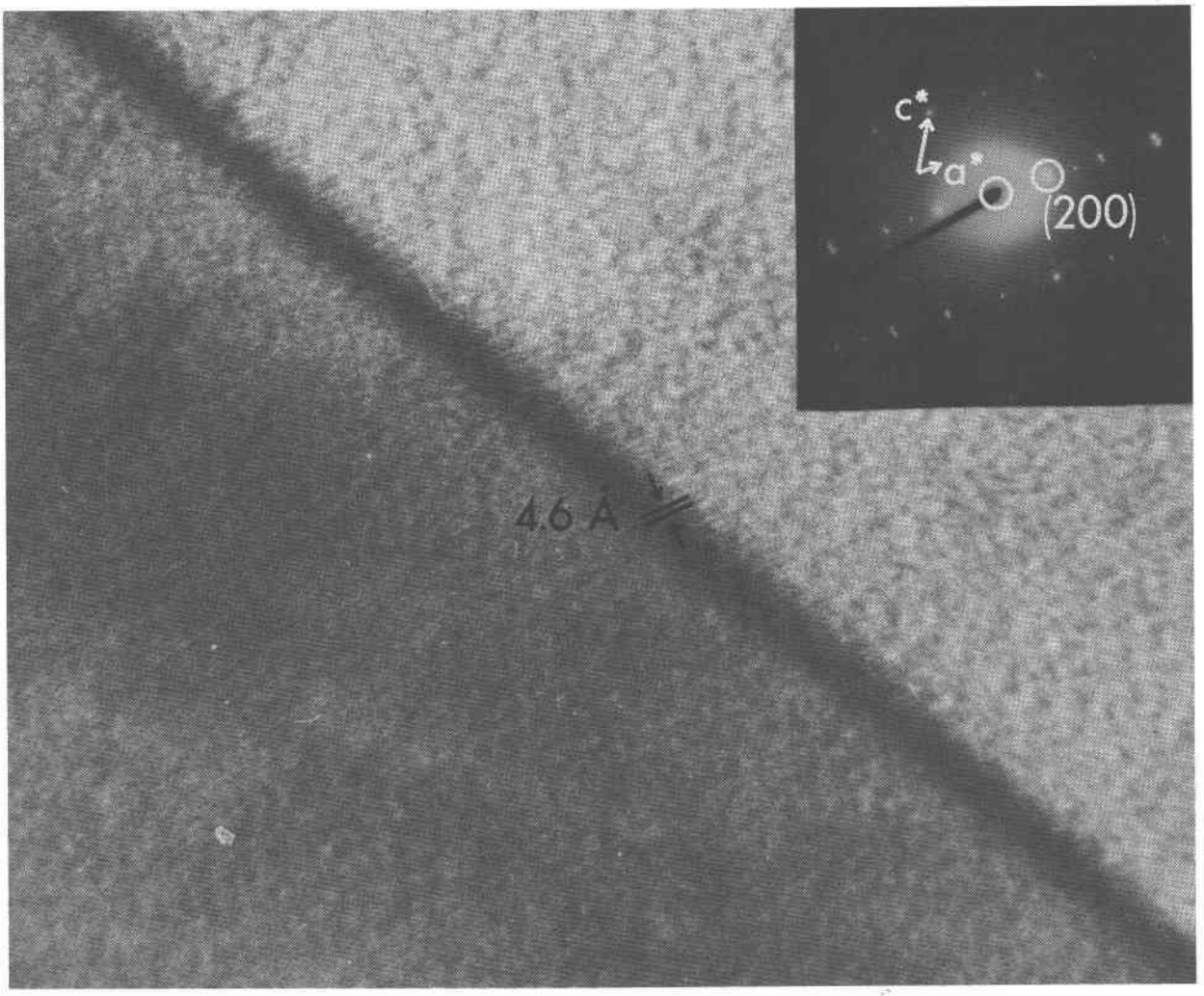

Fig. 6. Lattice fringe image of interphase boundary (001). Diffraction pattern (inset) shows the **a*c*** plane; circled are the central beam and the (200) reflection used to image the lattice fringes. Note the slight bending of the (200) planes across the interface. Dark-field micrograph, 100 kV.

indicates that the *a* and *b* parameters of both phases must have been as similar at the time of exsolution as they are now. In general, the exsolution relationships exhibited by the Balmat clinopyroxene provide markers in the cooling history of the rock.

In sum, techniques of analytical electron microscopy have provided information complementary to that determined by the more conventional techniques of electron microprobe analysis and single crystal X-ray diffraction. The exsolution relationships for clinopyroxenes in the system $CaSiO_3$–$MnSiO_3$–$MgSiO_3$ are strikingly similar to those of the common rock-forming system $CaSiO_3$–$FeSiO_3$–$MgSiO_3$.

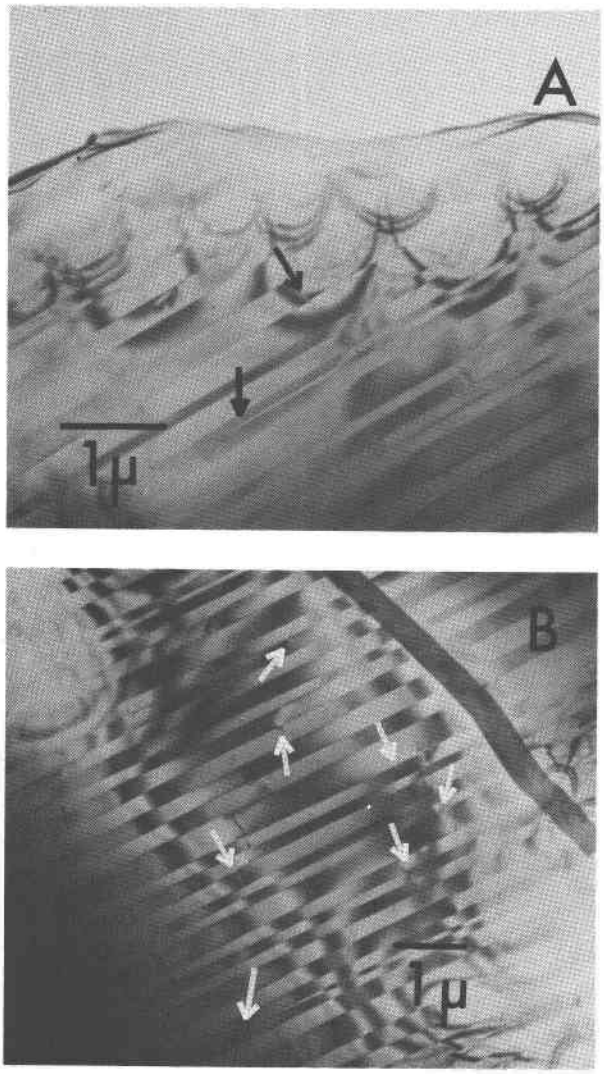

Fig. 7. Ledges (arrowed) along interphase boundary. "Pinch-out" lamella is arrowed in (A). Bright-field transmission micrographs, 100 kV.

Acknowledgments

We thank Professor W. C. Bigelow, John Mardinly, and Steve Krause of the Department of Materials and Metallurgical Engineering of The University of Michigan which houses the STEM and the electron microprobe for continuing operational assistance with the instruments and for many valuable discussions. We also thank Craig Johnson for the final electron microprobe analysis of the pyroxene. We are grateful to St. Joe Minerals Corporation who provided summer support for one of us (PEB), and particularly to Dr. David Dill who saw that the rhodonite- and pyroxene-bearing samples were saved. We are also indebted to Dr. Gordon L. Nord, Jr., of the U. S. Geological Survey for his careful review of the manuscript. This research was supported in part by a Sigma Xi Grant-in-Aid of Research and a Geological Society of America Research Grant to Wendy A. Gordon and NSF grant EAR 78-22758 to Donald R. Peacor.

References

Bailey, J. C., Champness, P. E., Dunham, A. C., Esson, J., Fyfe, W. S., MacKenzie, W. S., Stumpfl, E. F., and Zussman, J. (1970) Mineralogy and petrology of Apollo 11 lunar samples. Proceedings of the Apollo 11 Lunar Science Conference, 169–194.

Bohlen, S. R. and Essene, E. J. (1977) Feldspar and oxide thermometry of granulites in the Adirondack Highlands. Contributions to Mineralogy and Petrology, 62, 153–169.

Brown, G. E. and Wechsler, B. A. (1973) Crystallography of pigeonites from basaltic vitrophyre 15597. Proceedings of the Fourth Lunar Science Conference, 887–900.

Brown, G. E., Prewitt, C. T., Papike, J. J., and Sueno, S. (1972) A comparison of the structures of low and high pigeonite. Journal of Geophysical Research, 77, 5778–5789.

Brown, P. E., Essene, E. J., and Kelly, W. C. (1978) Sphalerite geobarometry in the Balmat-Edwards district, New York. American Mineralogist, 63, 250–257.

Brown, P. E., Essene, E. J., and Peacor, D. R. (1979) Phase relations inferred from field data for Ca–Mg–Mn pyroxenes and pyroxenoids. (abstr.) Transactions of the American Geophysical Union, 60, 422–423.

Busing, W. R., Martin, K. O., and Levy, H. A. (1964) A Fortran crystallographic function and error program. U. S. National Technical Information Service, ORNL-TM-306.

Carpenter, M. A. (1978) Nucleation of augite at antiphase boundaries in pigeonite. Physics and Chemistry of Minerals, 2, 237–251.

Champness, P. E. and Lorimer, G. W. (1971) An electron microscopic study of a lunar pyroxene. Contributions to Mineralogy and Petrology, 33, 171–183.

Christie, J. M., Lally, L. S. Heuer, A. H., Fisher, R. M., Griggs, D. T., and Radcliffe, S. V. (1971) Comparative electron petrography of Apollo 11, Apollo 12, and terrestrial rocks. Proceedings of the Second Lunar Science Conference, 69–80.

Clark, J. R., Appleman, D. E., and Papike, J. J. (1969) Crystal-chemical characterization of clinopyroxenes based on eight new structure refinements. Mineralogical Society of America Special Paper 2, 31–50.

Cliff, G. and Lorimer, G. W. (1972) The quantitative analysis of thin metal foils using EMMA-4—the ratio technique. Proceedings of the Fifth European Congress on Electron Microscopy, Institute of Physics, Bristol, p. 140–141.

Cliff, G. and Lorimer, G. W. (1975) The quantitative analysis of thin specimens. Journal of Microscopy, 103, 203–207.

Copley, P. A., Champness, P. E., and Lorimer, G. W. (1974) Electron petrography of exsolution textures in an iron-rich clinopyroxene. Journal of Petrology, 15, 41–57.

Cruickshank, D. W. J. (1965) Errors in least-squares methods. In J. S. Rollett, Ed., Computing Methods in Crystallography, p. 112–116. Pergamon Press, Oxford.

Cupschalk, S. G. and Brown, N. (1968) Kinetics of antiphase domain growth. Acta Metallurgica, 16, 657–666.

Doyle, P. A. and Turner, P. S. (1968) Relativistic Hartree–Fock X-ray and electron scattering factors. Acta Crystallographica, A24, 390–397.

Engel, A. E. J. (1956) Apropos the Grenville. In J. E. Thomson, Ed., The Grenville Problem, p. 74–76. Royal Society of Canada Special Publication 1.

Finger, L. W. and Prince, E. (1975) A system of Fortran IV computer programs for crystal structure computations. U. S. National Bureau of Standards, Technical Note 854.

Freed, R. L. and Peacor, D. R. (1967) Refinement of the crystal structure of johannsenite. American Mineralogist, 52, 709–720.

Ghose, S., Ng, G., and Walter, L. S. (1972) Clinopyroxenes from Apollo 12 and 14: exsolution, domain structure and cation order. Proceedings of the Third Lunar Science Conference, 507–531.

Ghose, S., Wan, C., and Okamura, F. P. (1975) Site preference and crystal chemistry of transition metal ions in pyroxenes and olivines. (abstr.) Acta Crystallographica, A31, S76.

Kobayashi, H. (1977) Kanoite, $(Mn^{++},Mg)_2[Si_2O_6]$, a new clinopyroxene in the metamorphic rock from Tatehira, Oshima Peninsula, Hokkaido, Japan. Journal of the Geological Society of Japan, 83, 537–542.

Lally, J. S., Heuer, A. H., Nord, Jr., G. L., and Christie, J. M. (1975) Subsolidus reactions in lunar pyroxenes: an electron petrographic study. Contributions to Mineralogy and Petrology, 51, 263–281.

Lally, J. S., Fisher, R. M., Christie, J. M., Griggs, D. T., Heuer, A. H., Nord, G. L., and Radcliffe, S. V. (1972) Electron petrography of Apollo 14 and 15 rocks. Proceedings of the Third Lunar Science Conference, 401–422.

Lorimer, G. W. and Champness, P. E. (1973) Combined electron microscopy and analysis of an orthopyroxene. American Mineralogist, 58, 243–248.

Morimoto, N. and Tokonami, M. (1969) Domain structure of pigeonite and clinoenstatite. American Mineralogist, 54, 725–740.

Morimoto, N., Appleman, D. E., and Evans, Jr., H. T. (1960) The crystal structures of clinoenstatite and pigeonite. Zeitschrift für Kristallographie, 144, 120–147.

Nobugai, K., Tokonami, M., and Morimoto, N. (1978) A study of subsolidus relations of the Skaergaard pyroxenes by analytical electron microscopy. Contributions to Mineralogy and Petrology, 67, 111–117.

Nord, Jr., G. L., Lally, J. S., Heuer, A. H., Christie, J. M., Radcliffe, S. V., Griggs, D. T., and Fisher, R. M. (1973) Petrologic study of igneous and metaigneous rocks from Apollo 15 and 16 using high voltage transmission electron microscopy. Proceedings of the Fourth Lunar Science Conference, 953–970.

Peacor, D. R. Essene, E. J. Brown, P. E., and Winter, G. A. (1978) The crystal chemistry and petrogenesis of a magnesian rhodonite. American Mineralogist, 63, 1137–1142.

Prewitt, C. T., Brown, G. E., and Papike, J. J. (1971) Apollo 12 clinopyroxenes: high temperature X-ray diffraction studies. Proceedings of the Second Lunar Science Conference, 59–68.

Ribbe, P. H. and Prunier, Jr., A. R. (1977) Stereochemical systematics of ordered $C2/c$ silicate pyroxenes. American Mineralogist, 62, 710–720.

Robinson, P., Jaffe, H. W., Ross, M., and Klein, Jr., C. (1971) Orientation of exsolution lamellae in clinopyroxenes and clinoamphiboles: consideration of optimal phase boundaries. American Mineralogist, 56, 909–939.

Rucklidge, J. C. and Gasparrini, E. L. (1969) Specifications of a complete program for processing electron microprobe data: EMPADR VII. Department of Geology, University of Toronto, Toronto.

Shannon, R. D. and Prewitt, C. T. (1969) Effective ionic radii in oxides and fluorides. Acta Crystallographica, B25, 925–946.

Stephenson, D. A., Sclar, C. B., and Smith, J. V. (1966) Unit cell volumes of synthetic orthoenstatite and low clinoenstatite. Mineralogical Magazine, 35, 836–846.

Syono, Y., Akimoto, S., and Matusi, Y. (1971) High pressure transformations in zinc silicates. Journal of Solid State Chemistry, 3, 369–380.

Manuscript received, February 1, 1980;
accepted for publication, September 15, 1980.